


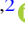






Dynamics and Morphology of Cold Gas in Fast, Radiatively Cooling Outflows: Constraining AGN Energetics with Horseshoes

Yu Qiu (邱宇)¹ , Haojie Hu^{1,2} , Kohei Inayoshi¹ , Luis C. Ho^{1,2} , Tamara Bogdanovic³ , and Brian R. McNamara^{4,5,6} 

¹ Kavli Institute for Astronomy and Astrophysics, Peking University, 5 Yiheyuan Road, Haidian District, Beijing 100871, People's Republic of China
yuqiu@pku.edu.cn

² Department of Astronomy, School of Physics, Peking University, 5 Yiheyuan Road, Haidian District, Beijing 100871, People's Republic of China

³ Center for Relativistic Astrophysics, School of Physics, Georgia Institute of Technology, 837 State Street, Atlanta, GA 30332, USA

⁴ Department of Physics and Astronomy, University of Waterloo, 200 University Avenue West, Waterloo, ON N2L 3G1, Canada

⁵ Waterloo Center for Astrophysics, University of Waterloo, 200 University Avenue West, Waterloo, ON N2L 3G1, Canada

⁶ Perimeter Institute for Theoretical Physics, Waterloo, ON N2L 2Y5, Canada

Received 2021 June 5; revised 2021 July 17; accepted 2021 July 20; published 2021 August 12

Abstract

Warm ionized and cold neutral outflows with velocities exceeding 100 km s^{-1} are commonly observed in galaxies and clusters. However, theoretical studies indicate that ram pressure from a hot wind, driven either by the central active galactic nucleus (AGN) or a starburst, cannot accelerate existing cold gas to such high speeds without destroying it. In this work we explore a different scenario, where cold gas forms in a fast, radiatively cooling outflow with temperature $T \lesssim 10^7 \text{ K}$. Using 3D hydrodynamic simulations, we demonstrate that cold gas continuously fragments out of the cooling outflow, forming elongated filamentary structures extending tens of kiloparsecs. For a range of physically relevant temperature and velocity configurations, a ring of cold gas perpendicular to the direction of motion forms in the outflow. This naturally explains the formation of transverse cold gas filaments such as the blue loop and the horseshoe filament in the Perseus cluster. Based on our results, we estimate that the AGN outburst responsible for the formation of these two features drove bipolar outflows with velocity $>2000 \text{ km s}^{-1}$ and total kinetic energy $>8 \times 10^{57} \text{ erg}$ about $\sim 10 \text{ Myr}$ ago. We also examine the continuous cooling in the mixing layer between hot and cold gas, and find that radiative cooling only accounts for $\sim 10\%$ of the total mass cooling rate, indicating that observations of soft X-ray and far-ultraviolet emission may significantly underestimate the growth of cold gas in the cooling flow of galaxy clusters.

Unified Astronomy Thesaurus concepts: Galaxy winds (626); Active galactic nuclei (16); Intracluster medium (858); Filamentary nebulae (535); Cooling flows (2028)

1. Introduction

Galactic winds and outflows are commonly observed in and around active galaxies (see Veilleux et al. 2005, for a review). Driven either by starbursts or accreting supermassive black holes (SMBHs), the velocity of such outflows ranges from $\lesssim 100$ to $\gtrsim 1000 \text{ km s}^{-1}$ (e.g., Filippenko & Sargent 1992), sometimes exceeding the sound speed of the outflowing material. The short destruction timescale of such outflows by strong shocks raises questions about the origin of the fast-traveling gas, as well as its subsequent evolution and interaction with the ambient medium. Two main branches of models have been proposed to explain the existence of the fast outflows.

1. On the one hand, cold gas may be entrained into a fast-moving hot wind (the so-called “cloud-crushing problem”, e.g., Klein et al. 1994; Cooper et al. 2009; Fujita et al. 2009; Scannapieco & Brüggén 2015; Gronke & Oh 2018; Sparre et al. 2019; Li et al. 2020; Kanjilal et al. 2021). However, this mechanism does not seem able to accelerate the bulk of the cold gas to velocities $>100 \text{ km s}^{-1}$ due to rapid shock destruction (Zhang et al. 2017), hindering its application to fast outflows.
2. On the other hand, cold gas may form within an initially hot, radiatively cooling outflow, which retains high speeds beyond $\sim 100 \text{ km s}^{-1}$ (Wang 1995; Thompson et al. 2016; Schneider et al. 2018; Qiu et al. 2020) and survives longer due to lower relative velocity with the original hot gas.

In this work we perform the first dedicated set of simulations to study the thermodynamical and morphological evolution of the cold gas that forms in a fast, initially hot, radiatively cooling outflow with short cooling time ($<10 \text{ Myr}$). In Section 2 we describe the simulation setup and the relevant observational constraints. Section 3 summarizes the dynamical evolution of the cold gas as well as the accompanying emission features. We then discuss the implications and conclude in Section 4.

2. Simulations of Radiatively Cooling Outflows

In order to facilitate the comparison with observations and demonstrate the applicability of the model, we initialize the simulations inside the deep potential well of a galaxy cluster, where both gravity and ram pressure from the ambient intracluster medium (ICM) play important roles in the dynamical evolution of the outflowing gas. Observationally, Russell et al. (2019) have measured 10^9 – $10^{11} M_{\odot}$ molecular gas in central cluster galaxies using Atacama Large Millimeter/submillimeter Array (ALMA) data. Most of the molecular gas lies in radial filamentary structures extending up to tens of kiloparsecs, with line-of-sight velocities below $\sim 500 \text{ km s}^{-1}$. The relatively low velocity and the widespread radial geometry have led to the postulation that the filaments are entrained by rising radio bubbles inflated by active galactic nucleus (AGN) jets (e.g., Revaz et al. 2008; McNamara et al. 2016). However, simulations performed by Duan & Guo (2018) revealed that the trailing cold gas is confined to the cluster core by gravity, unable to form extended filaments. Another

challenge facing past AGN feedback models is the presence of dust (e.g., Mittal et al. 2012), which cannot survive thermal sputtering (Draine & Salpeter 1979) if the cold gas forms due to thermal instabilities of the ambient hot ICM (e.g., Gaspari et al. 2012; McCourt et al. 2012; Li & Bryan 2014).

Using cluster-scale simulations that launch multiphase outflows from the central AGN (see Qiu et al. 2019b, and references therein for a detailed comparison of AGN feedback models), Qiu et al. (2020) proposed that the cold gas forms in radiatively cooling outflows with initial temperature $T \lesssim 10^7$ K. Because the cooling time ($\lesssim 10$ Myr) is shorter than the dust sputtering timescale (~ 10 Myr), and the timescale for the gas to reach maximum height (~ 100 Myr), the gas fragments into dusty cold clumps along the rising trajectory. Additionally, due to ram pressure from the intracluster plasma, the outflow speed is significantly decelerated before fragmentation, yielding cold gas velocities that are lower than predictions based on simple, ballistic estimates. Filaments formed in this way share properties similar to those observed in Perseus and other cool-core clusters (e.g., Conselice et al. 2001; Qiu et al. 2019a, 2019b).

Following the analytic model laid out in Qiu et al. (2020), we perform a series of 3D high-resolution simulations of a radiatively cooling outflow traveling radially in a cluster potential using the code ENZO (Bryan et al. 2014). The cluster is modeled after Perseus and initialized with hot plasma in hydrostatic equilibrium with the background gravity (contributed by the dark matter halo, the central galaxy, and the SMBH, as detailed in Qiu et al. 2019b). The outflowing gas, with temperature T_{out} and metallicity $Z=0.02$, is initially set up as a spherical clump in thermal pressure equilibrium with the surrounding ICM whose core temperature $T \approx 3 \times 10^7$ K, electron number density $n_e = 0.07 \text{ cm}^{-3}$, and a lower $Z=0.011$. The elevated metallicity of the outflowing gas allows us to model the transport of metals by the outflows (e.g., Kirkpatrick & McNamara 2015) and serves as a natural tracer for the outflowing gas. It also slightly increases the cooling rate of the outflow (by a factor between 1 and 2 depending on the gas temperature), but does not alter our results significantly. We fix the clump mass $M_{\text{out}} = 10^8 M_{\odot}$, in agreement with typical molecular gas clump measurements in Perseus (e.g., Salomé et al. 2006, 2008, 2011). The center of the clump is placed 1 kpc away from the SMBH along the x -axis. We then give the gas clump an initial outward velocity v_{out} , and follow its subsequent evolution for 40 Myr, which is roughly four times the cooling timescale.

We select the initial outflow velocity v_{out} based on the constraint that when cold gas fragments, the velocity is below 500 km s^{-1} (see model predictions in Figure 2). v_{out} is uniform within the clump, and aligned with the x -axis. As summarized in Table 1, we select two initial temperatures in order to investigate the different cold gas morphologies that can arise from the outflows, and note that $T_{\text{out}} \leq 10^7$ K outflows share similar filamentary structure, while $T_{\text{out}} > 1.3 \times 10^7$ K leads to net heating of the outflow, without forming cold gas in our simulations. The sound speed for $\sim 10^7$ K plasma is $\sim 500 \text{ km s}^{-1}$, which means the outflows explored in our simulations have Mach number of 2–4. Therefore, heating of the outflow is provided by a combination of shock heating and mixing with the entrained hot ICM. $T \approx 1.2 \times 10^7$ K represents the balance point between heating and radiative cooling, which leads to partial cold gas formation, as described in Section 3.

Table 1
Simulation Parameters

Simulation ID	Res. (pc)	v_{out} (km s^{-1})	T_{out} (10^7 K)	M_{out} (M_{\odot})
LTr	120	1200	1.0	10^8
LTmr	60	1200	1.0	10^8
LThr	30	1200	1.0	10^8
HTlr	120	2000	1.2	10^8
HTmr	60	2000	1.2	10^8
HThr	30	2000	1.2	10^8

Note. Simulation ID indicates the initial temperature of the outflowing clump, as well as the simulation resolution: low temperature (LT), high temperature (HT), low, medium, and high resolution (lr, mr, hr).

In order to explore the impact of simulation resolution, we perform three simulations with increasingly more refinement levels for each outflow temperature choice. The criteria for the adaptive mesh refinement include density, cooling time, Jeans length, and shocks (see Bryan et al. 2014; Qiu et al. 2019b, for more information). We model self-gravity of the gas in our simulations. This allows us to capture the shock-heated, radiatively cooling, and gravitationally collapsing gas in detail, but we note that the Jeans length of the cold, dense gas after it forms is not always resolved at the resolutions in our simulations (Truelove et al. 1997).

3. Dynamical Evolution of Cold Gas

In this section we present the simulation results of the radiatively cooling outflow as it decelerates by gravity and ram pressure, gradually loses thermal energy, and fragments into filaments of cold gas. In order to assess the simple analytic model laid out in Qiu et al. (2020), we also calculate and trace properties of the center of mass for the original outflowing gas in Section 3.2.

3.1. Spatial Distribution

We first examine the spatial distribution of the cold gas after it fragments out of the radiatively cooling plasma. With $T_{\text{out}} \approx 10^7$ K in the core of the simulated cluster, the cooling time of the outflow is ~ 10 Myr. In Figure 1 we show the projected neutral hydrogen column density, as well as the density-weighted line-of-sight velocity for three snapshots between 10 and 40 Myr for the representative, medium-resolution runs, LTmr and HTmr. In both cases, the cold gas first appears at $x = 10\text{--}20$ kpc, with hydrogen column densities $N_H \sim 10^{21}\text{--}10^{22} \text{ cm}^{-2}$. Before cooling to the neutral phase, the clump is significantly decelerated by the ram pressure from the core plasma, and the cold gas velocity along the direction of motion, v_x , is below 500 km s^{-1} . Subsequently, the gas fragments further by its self-gravity into smaller cold gas clumps. Throughout the 40 Myr evolution, the bulk of the cold gas never attained speeds higher than 500 km s^{-1} , in agreement with observational constraints (e.g., Gendron-Marsolaïs et al. 2018).⁷

The morphologies of the cold gas clumps, however, are different in these two cases. In LTmr, after the first generation

⁷ The SITELLE observation of the warm, ionized filaments emitting $\text{H}\alpha$ photons in the Perseus cluster (Gendron-Marsolaïs et al. 2018) reveals a rich velocity structure, including a low-velocity dispersion and a smooth velocity gradient along the length of the filaments. For brevity we defer the detailed comparison of the structures to a future work.

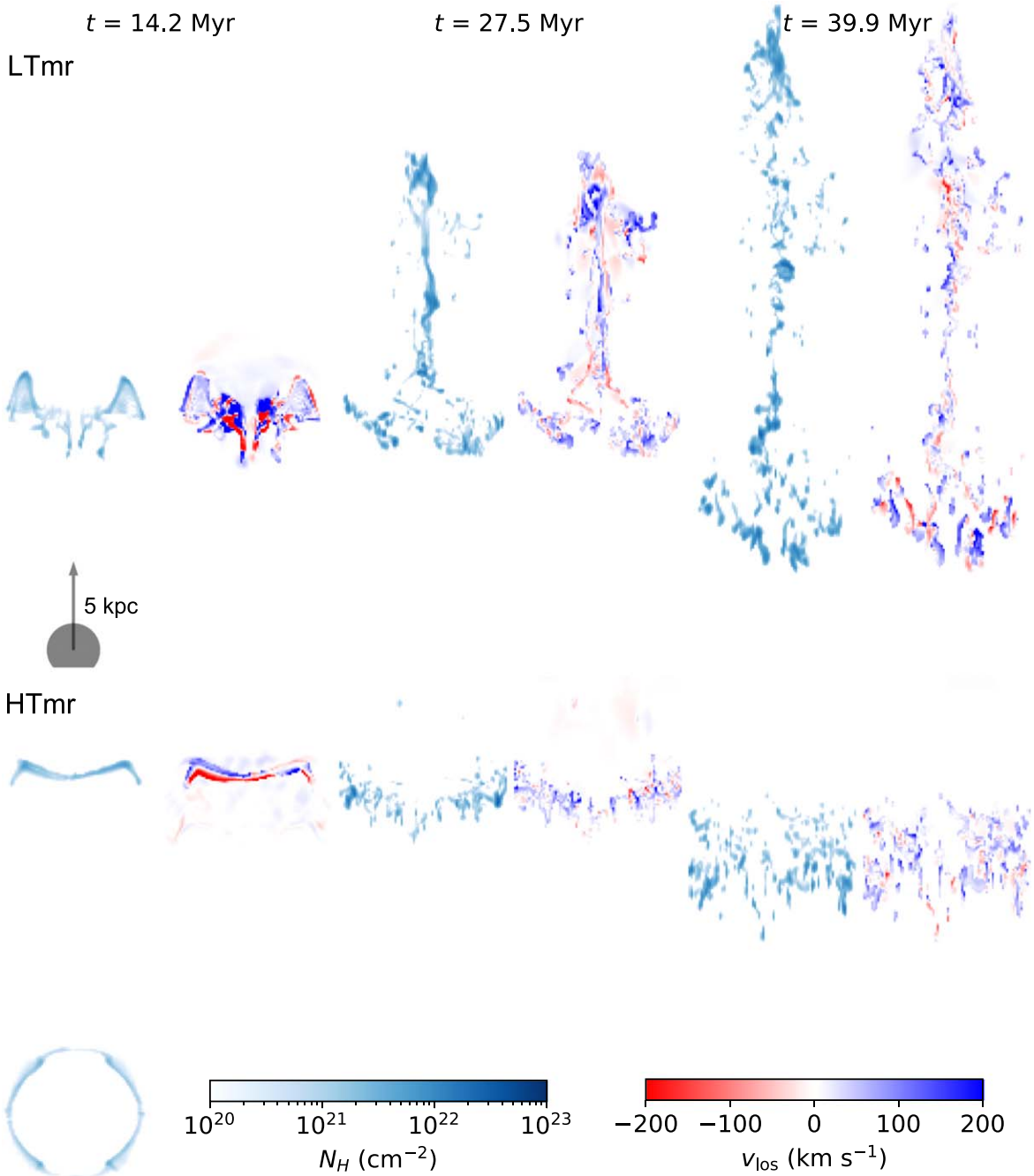


Figure 1. Spatial and velocity distribution of the cold gas that forms in the outflows, shown as projected neutral hydrogen column density, and mass-weighted line-of-sight velocity at three snapshots in the simulations LTmr and HTmr. Outflows are launched from the bottom of the panels with initial velocities upwards (shown by the gray circle and arrow). Projection along the flow direction that displays a ring structure is shown in the inset of the bottom-left panel.

of cold gas appears at the interface between the outflow and the ICM, ~ 15 kpc from the center, there is continuous cold gas formation in the remaining ionized outflow that rises to 40 kpc. By the end of the 40 Myr simulation, different generations of cold gas span over 10 kpc in length, with both positive and negative x -velocities. However, in HTmr with a slightly higher initial temperature, cold gas first appears as a ring on the outer edge of the outflowing clump due to increased density and elevated cooling (analogous to vortex rings in a turbulent fluid, e.g., the radio torus in M87, Owen et al. 2000; Churazov et al. 2001; Forman et al. 2017). The gas interior to the cold ring eventually penetrates through, but due to heating and mixing

with the entrained ICM, there is very little subsequent cold gas formation. Comparing these two simulations, the morphology of the cold gas depends sensitively on the initial condition of the outflow.

3.2. Comparison with the Analytic Model

The fragmentation and evolution of individual cold gas clumps are difficult to predict, but their collective behavior can be extracted for comparison with the analytic model. In Figure 2 we plot the evolution of v_x as a function of x -location for the center of mass of the initial outflowing gas, overlaid on top of the model prediction proposed in Qiu et al. (2020) for

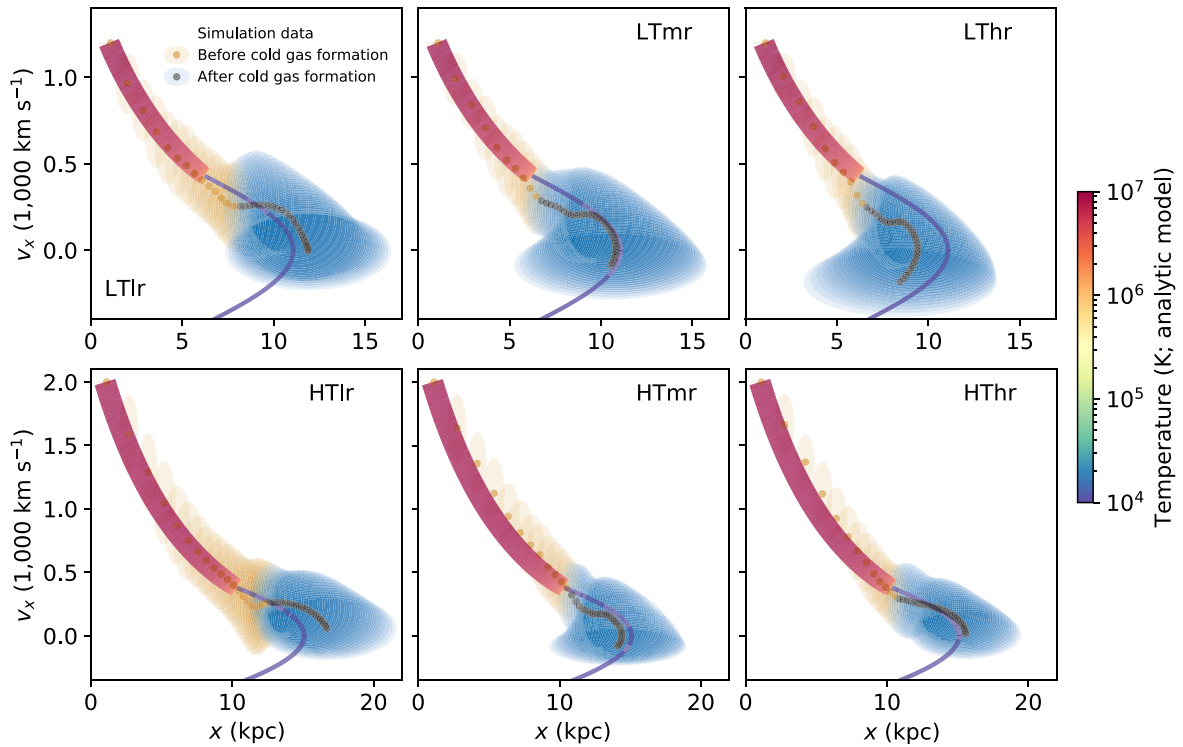


Figure 2. v_x evolution as a function of x -location of the outflowing gas traced by the elevated metallicity, sampled every ≈ 1 Myr. Orange and black circles represent the location and velocity of the center of mass of the outflow. The color changes after cold gas forms in the outflow. Orange and blue ellipses centered on each data point represent the standard deviation of the properties of the traced gas. Data points are overlaid on top of the analytic model from Qiu et al. (2020). The color and width of the lines represent the temperature and relative size of the outflowing clump.

each simulation. The analytic model assumes a sphere of outflowing clump is traveling in the cluster potential, and in thermal pressure equilibrium with the ICM. In each timestep it calculates the radiative cooling rate (Schure et al. 2009), the deceleration by gravity and ram pressure from the ICM, and updates the temperature, velocity, location, and size (cross section) of the outflowing clump. The original outflow in the simulations is traced by the elevated metal content in the gas cells. Each data point, sampled every ~ 1 Myr, is surrounded by an ellipse, whose vertical and horizontal axes represent the mass-weighted standard deviation of the gas velocity and position. This allows us to visualize the span of the individual cold gas clumps in both real and velocity space. The color of the ellipse changes from orange to blue after cold gas forms in the outflow.

Overall the evolution of the outflowing gas in the (x, v_x) diagram agrees with the analytic model. In the first ~ 10 Myr, the outflow cools radiatively and is decelerated to speeds $< 500 \text{ km s}^{-1}$. After cold gas forms, effects from the ram pressure diminishes, and the subsequent evolution can be described by a ballistic trajectory. Due to the faster initial speed in HT simulations, the center of mass reaches 15 kpc away from the cluster center, further than LT simulations. In both cases, the standard deviation of the gas velocity ($\lesssim 200 \text{ km s}^{-1}$, in agreement with Gendron-Marsolais et al. 2018) is much lower compared with the launching speed ($> 1000 \text{ km s}^{-1}$).

Apart from physical processes, simulation resolution also alters the distribution of the gas, but to a lesser degree. In both LT and HT cases, higher resolution leads to higher gas density that boosts the local radiative cooling rate of the ionized plasma. This results in earlier cold gas formation in medium- and high-resolution simulations compared with low-resolution runs. In addition, gas in

low-resolution simulations also tends to travel further, due to less turbulent motions developed on a coarser grid. However, simulation HTmr slightly breaks the trend with a lower height in the cluster atmosphere compared with HThr. As mentioned in Section 3.1, in HTmr the cold gas forms a ring, and the rest of the outflow continues to rise and mix with the surrounding ICM. This leads to a center of mass location that is larger than the spatial reach of the cold gas (as shown in Figure 1). The hot and rising outflow is again subject to ram pressure deceleration, thus reducing the ultimate spatial reach of the center of mass. The same ring structure does not appear in HThr, due to boosted radiative cooling with higher densities, leading to a cold gas distribution similar to that shown for LTmr in Figure 1. However, we do not seek resolution convergence for the gas morphology in this work, because physical processes not explored in our hydrodynamic simulations likely stabilize the cold gas against fragmentation, such as magnetic fields, conduction, and self-shielding (e.g., Li et al. 2020). HTmr represents a unique case in the explored parameter space, which indicates that the initial conditions and environmental properties must be very stringent for the ring structure to appear.

3.3. Radiative Cooling versus Mixing

Observationally, the cold gas embedded in the hot ICM is surrounded by a mixing layer of gas with soft X-ray ($\sim 0.5 \text{ keV}$, e.g., Fabian et al. 2006) and far-ultraviolet (FUV) emission (e.g., O VI emission from $T \sim 10^{5.5} \text{ K}$ gas; Bregman et al. 2006). Whether the plasma is cooling primarily radiatively or through non-radiative mixing⁸ with the cold gas complicates

⁸ Note here “non-radiative” refers to the bypass of X-ray and FUV emission. The mixed gas may still emit photons at lower energies.

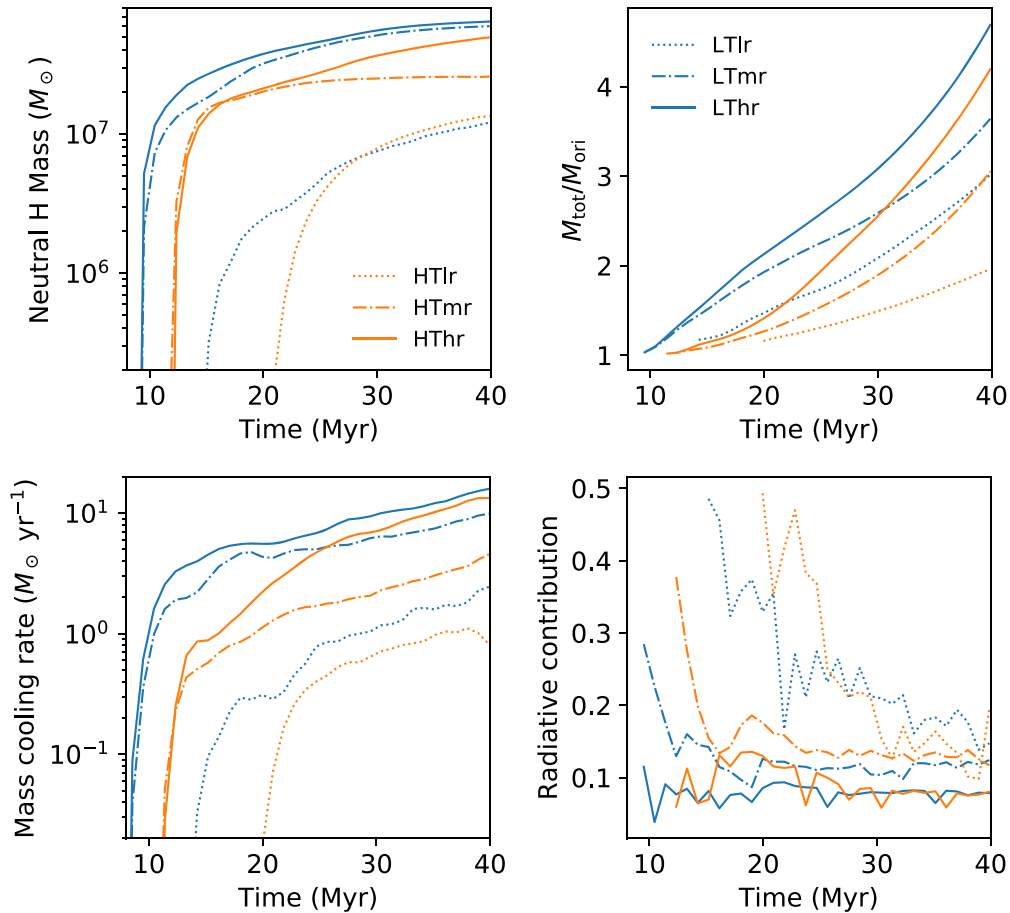


Figure 3. Evolution of the cold gas mass and mass cooling rate in simulations. Top-left panel: total amount of cold gas in the simulation traced by neutral hydrogen. Top-right panel: ratio between total cold gas (M_{tot}) and the component from the original outflow (M_{ori}). The increasing ratio indicates additional cold gas formation from the ICM. Bottom-left panel: total cold gas formation rate contributed by both radiative cooling and non-radiative mixing. Bottom-right panel: fraction of mass cooling rate inferred from the X-ray emissivity of the plasma with temperature between 10^6 – 10^7 K. Contribution by radiative cooling only accounts for 10% to 20% of the total mass cooling rate.

the interpretation of its emission features and mass estimates. In this subsection we compare the two cooling processes and access their relative significance in our simulations.

The top-left panel of Figure 3 shows the evolution of the cold gas mass in all six simulations, represented by their neutral hydrogen content, ranging between $M_{\text{tot}} \sim 10^6$ and $10^8 M_{\odot}$. Due to unresolved dense gas in low-resolution simulations, the final cold gas mass is lower by a factor of a few compared with medium- and high-resolution simulations. Using the elevated metallicity as a tracer, we also identify the component within the cold gas that originates from the initial outflowing gas (M_{ori}). Shown in the top-right panel, the ratio of total-to-original cold gas mass evolves from ≈ 1 when cold gas first appears around 10 Myr, to ≈ 2 – 4 toward the end of the simulations, indicating that the cold gas is constantly mixing with the ambient medium.

In order to separate the two cooling processes that can lead to the continuous growth of cold gas in our simulations, in the bottom panels of Figure 3 we compare the additional cold gas formation rate through mixing, $d(M_{\text{tot}} - M_{\text{ori}})/dt$, and the radiative cooling rate in the mixing layer between hot and cold gas. The radiative cooling rate is calculated by the thermal X-ray emission from gas with temperature $10^6 \text{ K} < T < 10^7 \text{ K}$ using the pyXSIM package (ZuHone et al. 2014), and then converting to mass cooling rates assuming an average plasma temperature of $5 \times 10^6 \text{ K}$. This reveals that the radiative cooling rate is lower

than the mixing cooling rate by a factor close to 10. Applying this ratio to real clusters and boosting the cold gas mass from $10^8 M_{\odot}$ to a typical $10^{10} M_{\odot}$, our analysis indicates that while the mass cooling rate inferred by soft X-ray and FUV emission is on the order of $\sim 10 M_{\odot} \text{ yr}^{-1}$ (Bregman et al. 2006; Fabian et al. 2006), cooling through non-radiative mixing between hot and cold gas can be 10 times faster. We caution, however, that the high mixing cooling rate may be due to insufficient simulation resolution, as discussed in Qiu et al. (2021).

4. Discussion and Application

In this work we perform the first hydrodynamic simulations to examine the dynamical and morphological evolution of cold gas that cools and fragments in an initially hot, radiatively cooling outflow in a galaxy cluster. Cold gas that forms in this way naturally retains the high speeds of the outflow $> 100 \text{ km s}^{-1}$, which helps explain the abundance of fast neutral and warm ionized gas observed in galaxies and clusters. We summarize the main results and implications below.

1. Continuous cold gas formation in the fast, radiatively cooling outflow results in a distribution of the gas along the direction of motion, which naturally explains the ~ 10 -kpc-long cold gas filaments commonly observed in cool-core clusters. Due to ram pressure deceleration in the cluster environment, the cold gas velocity is significantly

reduced before formation to speeds between 100 and 500 km s⁻¹ (Qiu et al. 2020), in line with observational constraints.

2. Under certain physically plausible conditions where heating balances radiative cooling, a ring of cold gas perpendicular to the direction of motion may form out of the outflowing gas. This is similar to the blue loop and the horseshoe filament in the Perseus cluster (e.g., Fabian et al. 2006), the latter was thought to be lifted by rising X-ray cavities (Fabian et al. 2003). These two features are located on opposite sides of the central AGN, indicating that they may be driven by the same AGN outburst 10–20 Myr ago that pushed out $\sim 10^8 M_\odot$ (Salomé et al. 2008, 2011) of radiatively cooling outflow in each direction. Assuming the initial outflow speed is >2000 km s⁻¹, as found in simulation HTmr, and the duration of the outburst is ~ 1 Myr, this implies a total kinetic energy $>8 \times 10^{57}$ erg, and an average AGN kinetic feedback power $\gtrsim 2 \times 10^{44}$ erg s⁻¹. Hence, properties of the cold gas filaments in galaxy clusters can be used to probe past AGN activity (see also Qiu et al. 2019a).
3. Adopting the outflow-to-accretion mass-loading factor $m = 200\text{--}500$ found in Qiu et al. (2021) for AGNs in giant elliptical galaxies, the $2 \times 10^8 M_\odot$ outflow estimated above also indicates that the central SMBH accreted at least $4 \times 10^5 M_\odot$ during the feeding episode. Assuming 10% feedback efficiency (Churazov et al. 2005), this yields a total energy output of $\sim 10^{59}$ erg, primarily in hot outflows exceeding 10^8 K that are difficult to detect with existing X-ray data (Qiu et al. 2021). Apart from heating the ICM, if a fraction of the cold gas driven by the central AGN collapses and forms stars, such as in the blue loop of the Perseus cluster (Fabian et al. 2008; Canning et al. 2010), this provides a channel for SMBHs to positively contribute to the star formation in giant elliptical galaxies, albeit delayed by ~ 10 Myr.
4. The mixing layer between hot and cold gas contributes significantly to the mass growth rate of the cold gas, tripling the gas content in 30 Myr. In comparison, the radiative cooling rate in the mixing layer is ~ 10 times lower. This indicates that the hot plasma may be cooling non-radiatively at a much faster rate than inferred from X-ray and FUV observations in the cooling flow of galaxy clusters, without additional local processes to heat or isolate the cold gas.

Our simulations of radiatively cooling outflows assume initial thermal pressure equilibrium between the outflow and the ICM, which fixes the initial density and cooling rate of the outflow for a given temperature. In real clusters, the pressure of the outflows may fluctuate around the equilibrium value and change the radiative cooling rate by a significant factor. Our parameter choice thus represents an intermediate scenario and provides a baseline for connecting AGN activity with the distribution of the cold gas in galaxies and clusters.

This work is supported by the National Key R&D Program of China (2016YFA0400702), the National Natural Science Foundation of China (11721303, 11991052, 11950410493, 12003003, 12073003), the China Postdoctoral Science Foundation (2020T130019), and the High-Performance Computing Platform of Peking University.

ORCID iDs

Yu Qiu (邱宇)  <https://orcid.org/0000-0002-6164-8463>
 Haojie Hu  <https://orcid.org/0000-0003-3143-3995>
 Kohei Inayoshi  <https://orcid.org/0000-0001-9840-4959>
 Luis C. Ho  <https://orcid.org/0000-0001-6947-5846>
 Tamara Bogdanović  <https://orcid.org/0000-0002-7835-7814>
 Brian R. McNamara  <https://orcid.org/0000-0002-2622-2627>

References

- Bregman, J. N., Fabian, A. C., Miller, E. D., & Irwin, J. A. 2006, *ApJ*, 642, 746
 Bryan, G. L., Norman, M. L., O’Shea, B. W., et al. 2014, *ApJS*, 211, 19
 Canning, R. E. A., Fabian, A. C., Johnstone, R. M., et al. 2010, *MNRAS*, 405, 115
 Churazov, E., Brügggen, M., Kaiser, C. R., Böhringer, H., & Forman, W. 2001, *ApJ*, 554, 261
 Churazov, E., Sazonov, S., Sunyaev, R., et al. 2005, *MNRAS*, 363, L91
 Conselice, C. J., Gallagher, John S., I., & Wyse, R. F. G. 2001, *AJ*, 122, 2281
 Cooper, J. L., Bicknell, G. V., Sutherland, R. S., & Bland-Hawthorn, J. 2009, *ApJ*, 703, 330
 Draine, B. T., & Salpeter, E. E. 1979, *ApJ*, 231, 77
 Duan, X., & Guo, F. 2018, *ApJ*, 861, 106
 Fabian, A. C., Johnstone, R. M., Sanders, J. S., et al. 2008, *Natur*, 454, 968
 Fabian, A. C., Sanders, J. S., Crawford, C. S., et al. 2003, *MNRAS*, 344, L48
 Fabian, A. C., Sanders, J. S., Taylor, G. B., et al. 2006, *MNRAS*, 366, 417
 Filippenko, A. V., & Sargent, W. L. W. 1992, *AJ*, 103, 28
 Forman, W., Churazov, E., Jones, C., et al. 2017, *ApJ*, 844, 122
 Fujita, A., Martin, C. L., Mac Low, M.-M., New, K. C. B., & Weaver, R. 2009, *ApJ*, 698, 693
 Gaspari, M., Ruszkowski, M., & Sharma, P. 2012, *ApJ*, 746, 94
 Gendron-Marsolais, M., Hlavacek-Larrondo, J., Martin, T. B., et al. 2018, *MNRAS*, 479, L28
 Gronke, M., & Oh, S. P. 2018, *MNRAS*, 480, L111
 Kanjilal, V., Dutta, A., & Sharma, P. 2021, *MNRAS*, 501, 1143
 Kirkpatrick, C. C., & McNamara, B. R. 2015, *MNRAS*, 452, 4361
 Klein, R. I., McKee, C. F., & Colella, P. 1994, *ApJ*, 420, 213
 Li, Y., & Bryan, G. L. 2014, *ApJ*, 789, 153
 Li, Z., Hopkins, P. F., Squire, J., & Hummels, C. 2020, *MNRAS*, 492, 1841
 McCourt, M., Sharma, P., Quataert, E., & Parrish, I. J. 2012, *MNRAS*, 419, 3319
 McNamara, B. R., Russell, H. R., Nulsen, P. E. J., et al. 2016, *ApJ*, 830, 79
 Mittal, R., Oonk, J. B. R., Ferland, G. J., et al. 2012, *MNRAS*, 426, 2957
 Owen, F. N., Eilek, J. A., & Kassim, N. E. 2000, *ApJ*, 543, 611
 Qiu, Y., Bogdanović, T., Li, Y., & McDonald, M. 2019a, *ApJL*, 872, L11
 Qiu, Y., Bogdanović, T., Li, Y., McDonald, M., & McNamara, B. R. 2020, *NatAs*, 4, 900
 Qiu, Y., Bogdanović, T., Li, Y., Park, K., & Wise, J. H. 2019b, *ApJ*, 877, 47
 Qiu, Y., McNamara, B. R., Bogdanovic, T., Inayoshi, K., & Ho, L. C. 2021, arXiv:2103.06505
 Revaz, Y., Combes, F., & Salomé, P. 2008, *A&A*, 477, L33
 Russell, H. R., McNamara, B. R., Fabian, A. C., et al. 2019, *MNRAS*, 490, 3025
 Salomé, P., Combes, F., Edge, A. C., et al. 2006, *A&A*, 454, 437
 Salomé, P., Oonk, J. B. R., Revaz, Y., et al. 2008, *A&A*, 484, 317
 Salomé, P., Combes, F., Revaz, Y., et al. 2011, *A&A*, 531, A85
 Scannapieco, E., & Brügggen, M. 2015, *ApJ*, 805, 158
 Schneider, E. E., Robertson, B. E., & Thompson, T. A. 2018, *ApJ*, 862, 56
 Schure, K. M., Kosenko, D., Kaastra, J. S., Keppens, R., & Vink, J. 2009, *A&A*, 508, 751
 Sparre, M., Pfrommer, C., & Vogelsberger, M. 2019, *MNRAS*, 482, 5401
 Thompson, T. A., Quataert, E., Zhang, D., & Weinberg, D. H. 2016, *MNRAS*, 455, 1830
 Truelove, J. K., Klein, R. I., McKee, C. F., et al. 1997, *ApJL*, 489, L179
 Veilleux, S., Cecil, G., & Bland-Hawthorn, J. 2005, *ARA&A*, 43, 769
 Wang, B. 1995, *ApJ*, 444, 590
 Zhang, D., Thompson, T. A., Quataert, E., & Murray, N. 2017, *MNRAS*, 468, 4801
 ZuHone, J. A., Biffi, V., Hallman, E. J., et al. 2014, arXiv:1407.1783